

Simultaneous analysis of SDSS spectra and GALEX photometry with STARLIGHT: Method and early results

A. Werle,^{1*} R. Cid Fernandes,¹ N. Vale Asari,^{1,2,3} G. Bruzual,⁴ S. Charlot⁵,
R. Gonzalez Delgado⁶ and F. R. Herpich^{1,7}

¹*Departamento de Física - CFM - Universidade Federal de Santa Catarina, Florianópolis, SC, Brazil*

²*School of Physics and Astronomy, University of St Andrews, North Haugh, St Andrews KY16 9SS, UK*

³*Royal Society–Newton Advanced Fellowship*

⁴*Instituto de Radioastronomía y Astrofísica, Universidad Nacional Autónoma de México, Morelia, Michoacán, 58089 México*

⁵*Sorbonne Universités, UPMC-CNRS, UMR7095, Institut d’Astrophysique de Paris, F-75014, Paris, France*

⁶*Instituto de Astrofísica de Andalucía (CSIC), Granada, Spain*

⁷*Instituto de Astronomia, Geofísica e Ciências Atmosféricas, Universidade de São Paulo, R. do Matão 1226, 05508-090 São Paulo, Brazil*

Accepted XXX. Received YYY; in original form ZZZ

ABSTRACT

We combine data from the Sloan Digital Sky Survey and the Galaxy Evolution Explorer to simultaneously analyze optical spectra and ultraviolet photometry of 231643 galaxies with the STARLIGHT spectral synthesis code using state-of-the-art stellar population models. We present a new method to estimate GALEX photometry in the SDSS spectroscopic aperture, which proves quite reliable if applied to large samples. In agreement with previous experiments with CALIFA, we find that adding UV constraints leads to a moderate increase on the fraction of $\sim 10^7 - 10^8$ yr populations and a concomitant decrease of younger and older components, yielding slightly older luminosity weighted mean stellar ages. These changes are most relevant in the low-mass end of the blue cloud. An increase in dust attenuation is observed for galaxies dominated by young stars. We investigate the contribution of different stellar populations to the fraction of light in GALEX and SDSS bands across the UV-optical color-magnitude diagram. As an example application, we use this λ dependence to highlight differences between retired galaxies with and without emission lines. In agreement with an independent study by Herpich et al., we find that the former show an excess of intermediate age populations when compared to the later. Finally, we test the suitability of two different prescription for dust, finding that our dataset is best fitted using the attenuation law of starburst galaxies. However, results for the Milky Way extinction curve improve with decreasing τ_V , especially for edge-on galaxies.

Key words: galaxies: stellar content – galaxies: evolution – ultraviolet: galaxies

1 INTRODUCTION

The spectral energy distribution (SED) of galaxies encodes properties such as star-formation histories (SFH), stellar masses, metallicities, and dust attenuation. Stellar population synthesis techniques aim to extract this information by comparing the SEDs of galaxies with models.

SED synthesis methods can be divided into two broad categories: parametric (Chevallard & Charlot 2016; Carnall et al. 2018; Noll et al. 2009) and non parametric (or inverse) methods (Panter et al. 2003; Cid Fernandes et al. 2005; To-

jeiro et al. 2007; Ocvirk et al. 2006; Koleva et al. 2009; Cappellari 2017; Leja et al. 2017). The first compares galaxy spectra with a set of composite stellar population (CSP) models built by combining simple stellar population (SSPs) spectra according to prescribed star-formation and chemical enrichment histories. In contrast, the latter retrieves stellar population information without any assumptions about the functional form of the galaxy’s SFH (see Walcher et al. 2011 and Conroy 2013 for complete reviews).

The main advantage of parametric models is that they require less detailed spectral information to constrain physical properties. This allows them to be applied to broadband photometry, while the application of non-parametric population synthesis is usually restricted to λ -by- λ spectral fits

* E-mail: ariel@astro.ufsc.br

of the stellar continuum (i.e., excluding nebular emission). For the same reason, certain galaxy properties such as abundance patterns and the contribution of binary stars to the SED can currently only be investigated through parametric models. A particular asset of using broadband photometry to measure galaxy properties is that large photometric data-sets are publicly available across the entire electromagnetic spectrum, allowing for the analysis of panchromatic SEDs. Large databases of galaxy spectra, on the other hand, are only available in the optical region.

To combine the best of both worlds, the STARLIGHT spectral synthesis code (Cid Fernandes et al. 2005) was updated to simultaneously account for spectral and photometric information, allowing the analysis of panchromatic data while maintaining the detailed spectral constraints necessary for a non-parametric fit. This method was first applied by López Fernández et al. (2016) to simultaneously fit integrated spectra from the CALIFA survey (Sánchez et al. 2012) and photometry from the Galaxy Evolution Explorer (GALEX, Martin et al. 2007). We note that while STARLIGHT is the first non-parametric code to include this feature, some parametric codes described in the literature also allow for the combination of spectra and photometry (e.g. BEAGLE, Chevallard & Charlot 2016, and BAGPIPES Carnall et al. 2018).

Several characteristics make the ultraviolet (UV) a natural choice for the expansion of the wavelength coverage of STARLIGHT fits. The main one is that this wavelength range provides key information about emission from OB stars, objects that dominate the UV emission in most galaxies even when they do not leave major footprints in the optical. Indeed, López Fernández et al. (2016) find that STARLIGHT fits to optical spectra alone tend to overestimate UV fluxes due to small ($\sim 2\%$) fractions of optical light attributed to these young, hot stars. The UV also opens a window to other astrophysical problems, such as the UV upturn in elliptical galaxies and the shape of dust attenuation curves.

This work aims to extend the analysis of UV constraints with STARLIGHT to a combination of SDSS and GALEX data, taking advantage of a larger sample size. The paper is organized as follows: data sources and the procedure to match the data-sets are described in section 2. Novelty in the spectral synthesis method are presented in Section 3. Synthesis results are discussed in Section 4, with focus on the effect of UV data on the properties derived by STARLIGHT. Examples of applications of the dataset to astrophysical problems are shown in Section 5. Finally, Section 6 summarizes our results. Throughout this work, we assume a standard Λ CDM cosmology with $\Omega_M = 0.3$, $\Omega_\Lambda = 0.7$ and $h = 0.7$.

2 DATA AND SAMPLE

2.1 Data sources and sample selection

The work presented in this paper is based primarily on optical spectra from SDSS DR8 (York et al. 2000; Aihara et al. 2011) and on UV photometry from GALEX GR6 (Martin et al. 2007), measured in two bands: *NUV* (effective wavelength $\lambda_{\text{NUV}}^{\text{eff}} = 2267 \text{ \AA}$) and *FUV* ($\lambda_{\text{FUV}}^{\text{eff}} = 1516 \text{ \AA}$).

Our general sample contains 231643 galaxies from the

SDSS main galaxy sample with photometry in both GALEX bands. The sample was selected from the GALEX CasJobs (<http://galex.stsci.edu/casjobs/>) by matching the UV object closest to each of the SDSS sources within a $0.3''$ search radius. For most of the analysis, we use a subsample of 137979 galaxies with $z < 0.1$, as this ensures that the wavelength ranges covered by the GALEX filters do not deviate largely from their rest-frame values; we will refer to this subsample as our low- z sample.

SDSS spectra and the *NUV* and *FUV* magnitudes from GALEX constitute the main observational data for our analysis, but we also make use of SDSS *ugriz* photometry to estimate GALEX magnitudes in the SDSS spectroscopic aperture, as explained next.

2.2 Combining SDSS spectra and GALEX photometry

The main limitation to our analysis is the FWHM of the GALEX PSF ($4.6''$ for *NUV* and $5.4''$ for *FUV*), which is larger than the aperture on which SDSS spectra are collected ($1.5''$ in radius). Our strategy to circumvent this issue is to indirectly estimate the GALEX $1.5''$ magnitudes based on GALEX integrated photometry and the difference between total (m_{tot}) and fiber ($m_{1.5}$) magnitudes $\Delta m_{1.5} \equiv m_{\text{tot}} - m_{1.5}$ in the SDSS *ugriz* bands.

The main factor that influences $\Delta m_{1.5}$ is the fraction of the galaxy's area sampled by the fiber; a secondary but important factor is that $\Delta m_{1.5}$ is larger in bluer filters, reflecting the difference in color between the central regions of galaxies (bulges) and their integrated light. We also find that $\Delta m_{1.5}$ correlates weakly with galaxy morphology, and has no dependence on integrated color and absolute magnitude, indicating that $\Delta m_{1.5}$ is not a strong function of galaxy type. Moreover, there is a tight correlation between $\Delta m_{1.5}$ on different SDSS filters, indicating that the values of $\Delta m_{1.5}$ in one band can be used to estimate $\Delta m_{1.5}$ in other wavelengths.

The relation of $\Delta m_{1.5}$ with the mean wavelength of the filters $\langle \lambda \rangle$ is shown in Fig. 1 for three example galaxies. This relation was used to predict values for $\Delta m_{1.5}$ in the ultraviolet by fitting a straight line to the *ugriz* measurements and extrapolating it to the GALEX bands (dashed black lines). The lines were fitted using the BCES method (Akritas & Bershady 1996), as implemented in python by Nemmen et al. (2012). In this context, the offset of the fitted line acts as a first order correction that is equal for all bands and accounts for the fraction of total light sampled by the spectroscopic fiber, while the slope accounts for the aforementioned difference between central and integrated colors.

The UV magnitudes in the SDSS spectroscopic aperture are thus estimated from

$$\begin{aligned} NUV_{1.5} &= NUV_{\text{tot}} - \widehat{\Delta m}_{1.5}^{NUV} \\ FUV_{1.5} &= FUV_{\text{tot}} - \widehat{\Delta m}_{1.5}^{FUV}, \end{aligned} \quad (1)$$

where $\widehat{\Delta m}_{1.5}^{NUV}$ and $\widehat{\Delta m}_{1.5}^{FUV}$ are the estimated corrections to the *NUV* and *FUV* bands. Notice that these corrections are estimated for each individual galaxy using its own *ugriz* data. In these expressions NUV_{tot} and FUV_{tot} are the values of `NUV_MAG_AUTO` and `FUV_MAG_AUTO` in the GALEX catalog. The difference between kron photometry from GALEX

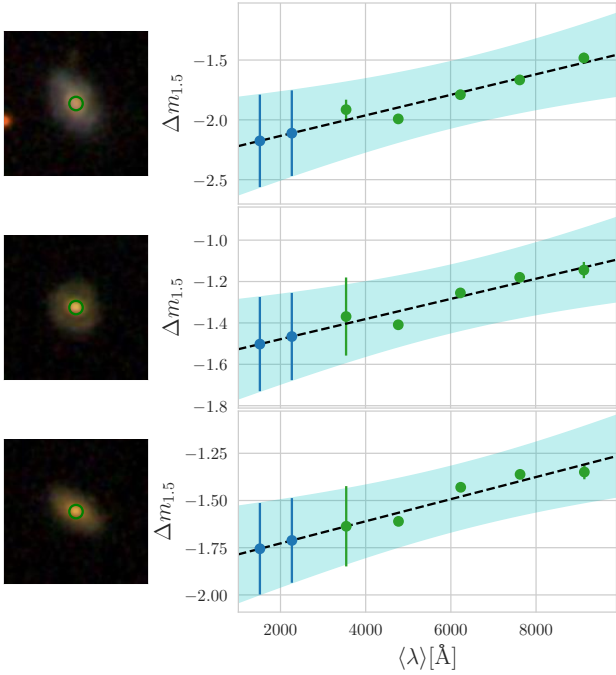


Figure 1. Examples of linear fits used to predict $\widehat{\Delta m}_{1.5}^{NUV}$ and $\widehat{\Delta m}_{1.5}^{FUV}$. Optical values of $\Delta m_{1.5}$ are plotted in green and the predicted values in blue. The best-fit linear relation is shown as a dashed line. The cyan band shows a $\pm 1\sigma$ prediction band, used to estimate the uncertainties in $\widehat{\Delta m}_{1.5}^{NUV}$ and $\widehat{\Delta m}_{1.5}^{FUV}$. The estimated error bars are plotted in blue. An image of the corresponding galaxy is shown to the left of each fit, with the region covered by the SDSS fiber indicated by a green circle.

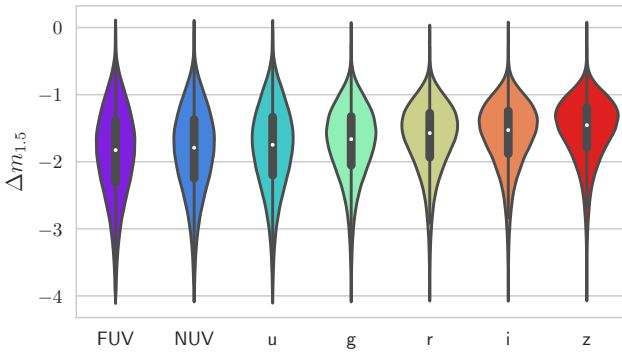


Figure 2. Violin plot of the distribution of $\Delta m_{1.5}$ in different bands. The distributions show measured values for SDSS and calculated values for GALEX. Box plots marking the medians and quartiles are shown inside each distribution.

and petrosian photometry from SDSS is very small and is therefore neglected.

Uncertainties in $\widehat{\Delta m}_{1.5}^{NUV}$ and $\widehat{\Delta m}_{1.5}^{FUV}$ are derived from the $\pm 1\sigma$ prediction bands for the fitted lines, as indicated in Fig. 1. These aperture matching uncertainties are added in quadrature to the errors in NUV_{tot} and FUV_{tot} to obtain the error in $NUV_{1.5}$ and $FUV_{1.5}$.

The distributions of $\Delta m_{1.5}^{NUV}$ and $\widehat{\Delta m}_{1.5}^{FUV}$ are compared

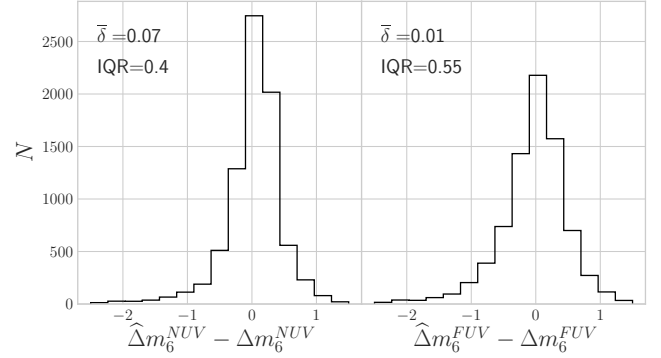


Figure 3. Comparison between predicted and measured values of Δm_6^{NUV} and Δm_6^{FUV} for a test sample of 6105 galaxies from the NASA-Sloan Atlas. Histograms show the differences between estimated and observed Δm_6 for *NUV* (left) and *FUV* (right) bands. Medians ($\bar{\delta}$) and interquartile regions (IQR) of the distributions are annotated in each panel.

to the observed $\Delta m_{1.5}$ for the *ugriz* bands in the violin plot in Fig. 2. A box plot showing median and quartiles is plotted inside each distribution. The distribution of the calculated $\Delta m_{1.5}$ for GALEX is very similar to the *u*-band, and shifted to larger (more negative) values than for other bands.

The median aperture corrections for the sample are -1.79 mag for *NUV* and -1.82 for *FUV*, while the median errors are 0.28 and 0.31 mag, respectively. We note, however, that since our method is completely unsupervised, it is expected to produce outliers, in particular for galaxies in close pairs or with odd morphological features. Indeed, in some cases the method returns unphysical values such as $\Delta m_{1.5} > 0$ (0.08% of the sample), as well as very high error estimates (larger than 1 mag in the *FUV* band for 0.07% of the sample). Ultimately, the reliability of our method depends on the linearity of the $\Delta m_{1.5} \times \langle \lambda \rangle$ relation. In cases where one or more bands deviate much from the linear trend the method is not reliable and will return high error estimates.

In order to test the reliability of our method, we use the GALEX-SDSS astrometry-matched radial profiles available in the NASA-Sloan Atlas (NSA, Blanton et al. 2011) to calculate the differences between the total magnitudes and that in an aperture of $6''$ in radius (Δm_6), where the image degradation caused by the GALEX PSF can be neglected. The idea behind this test is that $\Delta m_{1.5}$ can be thought of as the log of the ratio between total flux and the flux in the fiber, which is a relative quantity. Therefore, by choosing a larger aperture we can use nearby galaxies (with large projected radii) to mimic the distribution of $\Delta m_{1.5}$ in the general sample. With that in mind, we selected a test sample of 6105 galaxies with values of Δm_6 in the SDSS bands in the same range as the $\Delta m_{1.5}$ values for the general sample. Our method was then applied to estimate the values of Δm_6 for the test sample.

Results of this test are shown in the histograms of Fig. 3, where we plot the distributions of $\widehat{\Delta m}_6^{NUV} - \Delta m_6^{NUV}$ and $\widehat{\Delta m}_6^{FUV} - \Delta m_6^{FUV}$. The distributions are centered near zero, with medians of 0.07 mag for *NUV* and -0.01 for *FUV*. However, both distributions are quite wide, with interquartile regions of 0.4 on *NUV* and 0.55 on *FUV*. These statistics

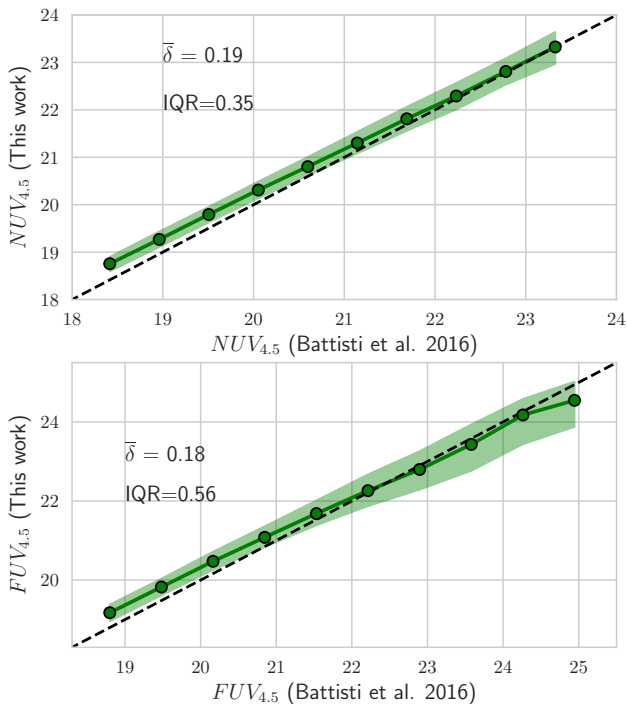


Figure 4. Comparison of UV magnitudes calculated by [Battisti et al. \(2016\)](#) with UV magnitudes calculated using the method of this paper for an aperture of radius $2.25''$. Green lines show median curves with the region between 25 and 75% percentiles is shaded in green. Median $y - x$ ($\bar{\delta}$) values and interquartile regions (IQR) are annotated on each panel.

confirm that our estimates are good for large samples, although results for individual sources may not be reliable.

We also used the NSA to calculate Δm in an aperture of $2.25''$ in radius, which allows us to compare our aperture matching scheme to the one of [Battisti et al. \(2016\)](#), that is calibrated in this aperture. This comparison is shown in Fig. 4. Magnitudes obtained with both methods are linearly correlated, although the method described here produces systematically dimmer magnitudes. Over the whole sample, the median difference between the methods is 0.19 magnitudes on NUV and 0.18 on FUV , the interquartile regions (IQR) are of 0.35 magnitudes on NUV and 0.56 on FUV , with a larger scatter for dimmer sources, specially in the FUV band. Considering that these two aperture matching schemes follow completely different routines and are even based on different data¹, the agreement between the predicted magnitudes is reassuring for both methods.

Despite the wide distributions of $\hat{\Delta}m_6^{NUV} - \Delta m_6^{NUV}$ and $\hat{\Delta}m_6^{FUV} - \Delta m_6^{FUV}$, the predicted values are, on average, in very good agreement with the observed ones. This is sufficient for the purpose of this paper, since all our results will be averaged in relatively large samples. Nonetheless, in some cases this process can yield corrections that deviate from the

¹ The correction from [Battisti et al. \(2016\)](#) uses a convolution of the galaxy’s Sérsic profile in the u band with the GALEX PSF to calculate scale factors that are applied to the GALEX $1.5''$ photometry.

distributions shown in Fig 2. To circumvent this we remove galaxies with corrections larger than 0 or smaller than -4 magnitudes in one of the GALEX bands, discarding 3300 galaxies (0.14% of the sample).

2.3 Preprocessing steps

Besides the aperture matching correction explained above, the data undergo a few pre-processing steps before being fed to STARLIGHT.

From DR7 onwards, SDSS spectra are calibrated to match the flux of a point source within one FWHM of the PSF, leading to fluxes typically 25% smaller than their photometric counterparts for extended sources. Due to this offset, calculating NUV and FUV fluxes compatible with fiber photometry does not directly ensure compatibility with spectroscopic fluxes. We have thus rescaled the SDSS spectra to match the $3''$ photometry in the r band, as done in the MPA/JHU value added galaxy catalog (www.mpa-garching.mpg.de/SDSS/DR7). Since the shape of the photometric SEDs is very similar to the shape of the spectra, this procedure ensures the compatibility of SDSS spectra with $ugriz$ fiber photometry and, by extension, with the estimated $NUV_{1.5}$ and $FUV_{1.5}$ estimated fiber magnitudes.

Both the optical spectra and UV photometry are corrected for Galactic extinction using the [Cardelli, Clayton & Mathis \(1989\)](#) extinction law with $R_V = A_V/E(B - V) = 3.1$, and $E(B - V)$ values from [Schlegel et al. \(1998\)](#) assuming the recalibration introduced in [Schlafly & Finkbeiner \(2011\)](#).

Finally, the spectra are shifted to $z = 0$ and re-sampled to 1\AA wavelength intervals. UV fluxes, however, are not k-corrected to rest-frame values. Instead, STARLIGHT uses the known redshift of the source to evaluate the predicted NUV and FUV magnitudes in the observed frame.

2.4 Ancillary data

The stellar population analysis presented in this work is based on the pre-processed SDSS spectra and GALEX magnitudes described in the previous sections. Even though no other data is required for this analysis, information on properties like emission lines and host morphology is key to the interpretation of the results. Following the statistical gist of this study, we will use such ancillary data to organize sources into different groups and examine the results in a comparative way. We use the Galaxy Zoo ([Lintott et al. 2008](#)) morphology to define subsamples of ellipticals and spirals. Emission line fluxes used in section 5.2 are drawn from [Mateus et al. \(2006\)](#).

The main method to group galaxies explored in this paper is the $NUV - r$ versus M_r color magnitude diagram (CMD). Unlike purely optical based CMDs, where the red sequence, blue cloud and green valley populations exhibit substantial overlap, this UV-optical CMD clearly represents the bimodality of the local galaxy population, making it a valuable tool to examine trends for different galaxy types ([Martin et al. 2007](#); [Salim 2014](#); [Gonçalves et al. 2012](#)). To build this CMD we calculated absolute magnitudes, which are corrected for Galactic extinction and k-corrected to $z = 0$ using the KCORRECT code ([Blanton & Roweis 2007](#)). We note that this is the only use of k-correction in this paper.

3 SPECTRAL SYNTHESIS

3.1 Method

The version of STARLIGHT used in this paper introduces a few novelties with respect to López Fernández et al. (2016), the main change being the scheme for combining photometric and spectroscopic figures of merit.

The spectroscopic and photometric parts of the χ^2 are defined as

$$\begin{aligned}\chi_{\text{SPEC}}^2 &= \sum_{\lambda} w_{\lambda}^2 (O_{\lambda} - M_{\lambda})^2 \\ \chi_{\text{PHO}}^2 &= \sum_{l=0}^{N_l} \left(\frac{m_l^{\text{obs}} - m_l^{\text{mod}}}{\sigma_l} \right)^2,\end{aligned}\quad (2)$$

where O_{λ} and M_{λ} are the observed and model spectra, w_{λ} is the inverse error in O_{λ} (except in bad pixels and regions around emission lines, which are discarded from the fits by setting $w_{\lambda} = 0$), l is an index corresponding to each of the N_l photometric filters, m_l^{obs} and m_l^{mod} are the observed and modeled AB magnitudes in filter l and σ_l are the errors in the magnitudes. Model magnitudes are calculated by performing synthetic photometry in the model spectrum M_{λ} after shifting it to the observed frame, ensuring consistency with the input apparent magnitudes m_l .

In all practical applications, N_l is much smaller than the number of spectroscopic data points N_{λ} – for instance, $N_l = 2$ and $N_{\lambda} \sim 4000$ in this paper. In order to simultaneously minimize χ_{SPEC}^2 and χ_{PHO}^2 , this scale difference has to be circumvented in our definition of the total χ^2 . Therefore, we define the total χ^2 as

$$\chi_{\text{TOT}}^2 = \chi_{\text{SPEC}}^2 + g_{\text{PHO}} \frac{N_{\lambda}}{N_l} \chi_{\text{PHO}}^2, \quad (3)$$

where g_{PHO} is a technical parameter that sets the relative weight of photometric and spectroscopic constraints.

López Fernández et al. (2016) did experiment with this recipe, but concluded that no scaling of χ_{PHO}^2 was necessary to adequately fit both their UV photometry and optical spectra. This is not, however, valid in general. In particular, the uncertainties in the spectroscopic and photometric fluxes play a central role in defining the balance between χ_{SPEC}^2 and χ_{PHO}^2 . Optimal values of g_{PHO} are thus dataset-dependent.

For the combination of SDSS spectra and aperture-corrected GALEX photometry used in this paper we find that g_{PHO} values of the order of 0.1 are necessary to adequately fit both the UV and optical data, so this is the value adopted throughout this work. Increasing g_{PHO} improves the fit of UV fluxes at the expense of degrading the quality of the fit of the optical spectrum (particularly in its blue end), and vice versa.

3.2 Stellar population base

Spectral synthesis with STARLIGHT depends on a few astrophysical ingredients, the main one being a base of stellar population spectra.

The base used in this paper is built from SSP models from Charlot & Bruzual (2018, in preparation, CB18 hereafter), which include considerable improvements upon the

Bruzual & Charlot (2003) models. The CB18 models incorporate the PARSEC evolutionary tracks computed by Chen et al. (2015) for 16 values of the stellar metallicity ranging from $Z = 0$ to $Z = 0.06$. These tracks include the evolution of the most massive stars losing their hydrogen envelope through the Wolf-Rayet (WR) phase, and have been complemented with the work by Marigo et al. (2013) to follow the evolution of stars through the thermally pulsing asymptotic giant branch (TP-AGB) phase. A large number of empirical and theoretical stellar libraries is used to describe the spectrophotometric properties of the stars along these tracks. For the age and wavelength ranges of interest for this paper, the dominant stellar spectra come in the visible range from the MILES stellar library (Sánchez-Blázquez et al. 2006; Falcón-Barroso et al. 2011) and in the UV range from the theoretical libraries computed by Lanz & Hubeny (2003a,b, 2007); Leitherer et al. (2010); Martins et al. (2005); Rodríguez-Merino et al. (2005); Rauch (2003), and the high resolution PoWR models (Sander et al. 2012; Hamann et al. 2006; Hainich et al. 2014, 2015; Todt et al. 2015; Gräfener et al. 2002; Hamann & Gräfener 2003) to describe stars in the WR phase. The effects of dust shells surrounding TP-AGB stars on their spectral energy distribution (Aringer et al. 2009; Rayner et al. 2009; Westera et al. 2002) is treated as in González-Lópezlira et al. (2010). The CB18 models have been used, among others, by Gutkin et al. (2016); Wofford et al. (2016); Vidal-García et al. (2017); Fritz et al. (2017); Bitsakis et al. (2017, 2018). These models are available to the interested user upon request. A comparison between the new models and the ones from Bruzual & Charlot (2003) is made in appendix A of Vidal-García et al. (2017). A more detailed comparison will be provided by CB18.

We use these SSP models to compute the spectra of CSPs resulting from periods of constant star formation rate. The age range from $t = 1$ Myr to 14 Gyr was divided onto 16 logarithmically spaced age bins. We use seven values of metallicity between $Z = 0.0005$ and $3.5Z_{\odot}$ ($Z_{\odot} = 0.017$), yielding a base of $16 \times 7 = 112$ CSPs.

3.3 Dust attenuation

The effects of dust attenuation² in this work are modeled as if produced by a single foreground screen which attenuates fluxes by a factor $e^{-\tau_{\lambda}}$, with τ_{λ} parameterized as the product of the optical depth in the V-band (τ_V) and a $q_{\lambda} \equiv \tau_{\lambda}/\tau_V$ attenuation or extinction curve.

We have performed spectral fits with two different recipes for q_{λ} : the MW law, as parameterized by Cardelli et al. (1989) with $R_V = 3.1$ (CCM), and the Calzetti et al. (2000) law (CAL), modified in the $\lambda < 1846 \text{ \AA}$ range to smoothly turn into the curve derived by Leitherer et al. (2002).³ The most notable difference between these laws is the presence or absence of the so called ‘UV bump’, a broad

² Throughout this paper, we adopt the standard definition of “extinction” as the scattering and absorption of photons out of the line of sight, while “attenuation” is defined as the combination of absorption and scattering in and out of the line of sight with local and global geometric effects.

³ This modification has only minor effects, restricted to the FUV band.

peak in q_λ around 2175 Å (Stecher 1965), within the range of the *NUV* filter. A more fundamental difference between them is that while CAL formally represents an attenuation law, CCM is originally an extinction curve, a crucial distinction when modeling the two processes (e.g Witt & Gordon 2000). In the context of this work, however, CCM is used to model attenuation, so the term ‘attenuation law’ may loosely apply. These two laws are chosen because they are the most often used in STARLIGHT-based work, and also because they allow us to test how an UV bump affects the fitting of UV data. These characteristics suit our central goal, which is to showcase the potential of the combined analysis of optical spectra and UV photometry with STARLIGHT.

A comparison of results obtained with the two laws is presented in section 5.3, but we anticipate that the best results for the general population of galaxies are obtained for the Calzetti law. Accordingly, all results presented up to section 5.3 assume this prescription.

4 SYNTHESIS RESULTS

Having discussed the sample, how we handle the data, and the method of analysis, this section presents the results of the synthesis. Throughout this section the emphasis is on the comparison of results obtained from purely optical spectral fits to SDSS data with those obtained with the addition of GALEX *NUV* and *FUV* photometry.

4.1 Spectral fits and UV magnitudes

Fig. 5 show examples of spectra fitted with and without photometric constraints for three different galaxies, ordered from red (top) to blue (bottom) *NUV*–*r* colors. The observed SDSS spectra are shown in black, except for regions masked because of bad pixels or emission lines, which are shown in yellow. Red and blue lines show the optical and combined optical + UV model fits, respectively. Observed UV fluxes are shown as black circles, while model values are plotted as orange circles for the optical-only fits and cyan for the optical + UV fits. All fluxes are relative to the flux at the normalization wavelength, set to $\lambda_0 = 5635\text{Å}$.

Fig. 5 confirms the results of López Fernández et al. (2016), in that purely optical fits tend to predict UV fluxes much larger than the observed ones. This happens because, as will be discussed next, optical-only fits can easily accommodate small contributions of very young stellar populations which hardly affect the optical fluxes, but become dominant at UV wavelengths. The addition of UV constraints allows STARLIGHT to successfully fit UV magnitudes with very little changes to the fitted optical spectra. Also, since this effect involves only small fractions of stellar mass and optical light, no drastic change is observed in the measured star-formation histories, as will become clear in Figs. 7 and 8.

This effect is further illustrated in Fig 6, where we plot histograms of the difference between the modeled and observed UV magnitudes for the full sample. For fits without photometric constraints, UV magnitudes are overshoot by 0.41 ± 0.91 magnitudes on *NUV* and 0.83 ± 1.32 on *FUV*, yielding values that are often brighter than the integrated UV magnitudes.

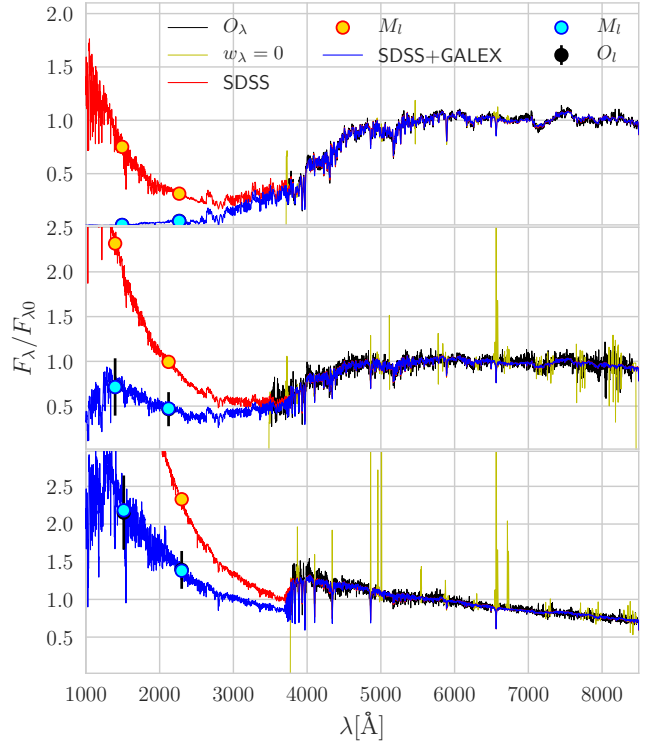


Figure 5. Examples of STARLIGHT fits for three galaxies in our sample. Black lines show optical spectra, with masked or flagged regions marked in green. Red lines show purely spectroscopic fits, while blue lines show combined UV + optical fits. Black circles with error bars mark the observed GALEX fluxes ($NUV_{1.5}$ and $FUV_{1.5}$, scaled to the SDSS aperture using the method described in Section 2.2), cyan circles are the fitted GALEX fluxes. Orange circles show UV fluxes predicted from purely optical fits. All fluxes are relative to the flux at 5635 Å.

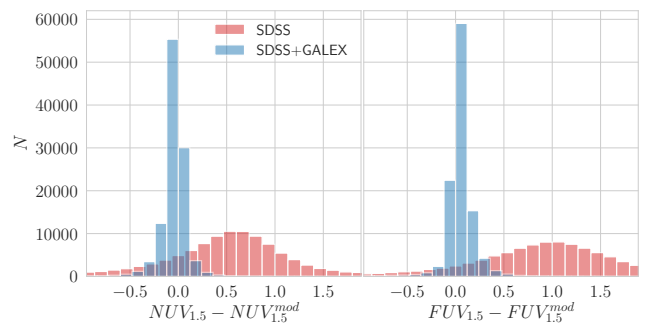


Figure 6. Histograms comparing differences between observed *NUV* (left) and *FUV* (right) magnitudes and the values predicted from optical spectra (red) and fitted from GALEX photometry (blue).

4.2 Star Formation Histories

We now examine the changes in the derived SFHs generated by the inclusion of UV constraints in the analysis. Within STARLIGHT SFHs are described in terms of the light fraction population vector \vec{x} , which quantifies the contribution of different base components to the observed flux at a nor-

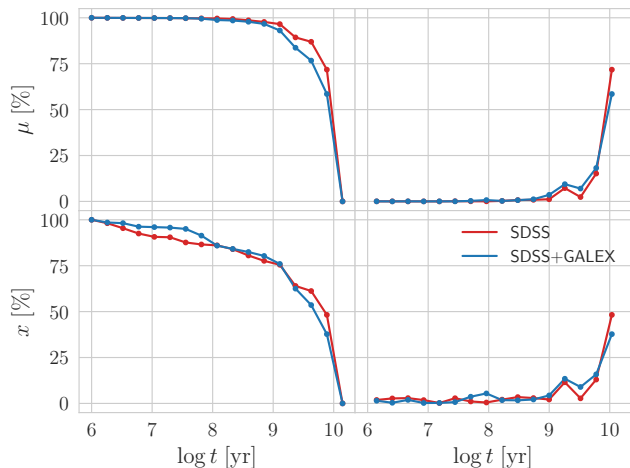


Figure 7. Average star formation histories calculated with and without photometric constraints. Top panels show cumulative (left) and non-cumulative (right) mass fractions as a function of age, while bottom panels show the corresponding curves in terms of light fractions at $\lambda_0 = 5635\text{\AA}$. Red lines show values for SDSS only STARLIGHT-fits and blue lines show values for SDSS+GALEX.

malization wavelength. The mass fraction vector $\vec{\mu}$ is derived from \vec{x} and the light-to-mass ratios of the base populations.

Fig. 7 shows the average \vec{x} and $\vec{\mu}$ vectors for all galaxies in our low z sample, obtained after collapsing the Z -axis (i.e., adding all components with same age but different metallicities). These distributions of mass and light with age are shown in both fractional (right panels) and cumulative forms (left).

The addition of UV data shifts light fractions from the $< 10^7$ yr populations to slightly older ones, from 10^7 to 10^8 yr, as can be seen in the bottom panels of Fig. 7. This is enough to prevent the overshooting of UV fluxes, but tends to produce a redder optical spectrum. To prevent this, STARLIGHT also removes contributions from the oldest stellar populations. The χ^2_{SPEC} values obtained with the addition of UV constraints are only marginally worse (by 3% on average) than those obtained with purely optical fits, confirming that the fitted optical spectra are kept essentially unchanged. When translating light fractions into mass fractions, the main difference between the two types of fits lies in the older populations: Fits with UV constraints show a slower and smoother build-up of stellar mass at early epochs.

The sample averaged SFHs in Fig. 7 mix very different kinds of galaxies, however. To get a sense of the diversity of SFHs in our sample and how they change with the addition of UV data, we calculated average light and mass fractions in bins across the $NUV-r$ vs. M_r color-magnitude diagram. In this diagram, and at the redshift limit of our sample, the blue cloud can be defined by the criterion of $NUV-r < 4$ and the red sequence by $NUV-r > 5$, while points in the $4 < NUV-r < 5$ range lie in the green valley (Salim 2014). On the assumption that sources in a given locus of the CMD can be considered intrinsically similar, these local averages are much less sensitive to sample selection effects. The results are plotted in Fig. 8.

The largest changes in SFH occur for galaxies in the

low-mass end of the blue cloud (bottom-right panels), where young stellar populations are more abundant and UV constraints are expected to play a larger role. The redistribution of $< 10^7$ and $> 10^9$ to 10^7 – 10^8 yr populations, which was the most noticeable change for the sample average, is very clear among these galaxies.

We also note that purely optical fits of red sequence galaxies (top panels) tend to wrongly identify very young populations ($t < 10$ Myr) at levels of order 2%. These are the fake young bursts first identified by (Ocvirk 2010, see also Cid Fernandes & González Delgado 2010). The addition of UV data constrains these populations, thus averting the problem.

Overall, the differences between SFHs calculated with and without UV data become smaller with redder colors and increasing luminosity, i.e., as the contribution of old stars increase. For light fractions, our results are similar to the ones obtained by López Fernández et al. (2016). For mass fractions, however, there are differences. While López Fernández et al. (2016) finds faster rising cumulative $\mu(> t)$ curves for optical+UV fits than with purely optical ones in blue cloud galaxies, here we observe a trend in the opposite direction (as best seen in panel w of Fig. 8). Besides the many differences in sample, data, aperture corrections, and optical/UV weighing scheme, the current fits differ in the base models, which employ different isochrones and stellar libraries. We have verified that using base models compatible with those used by López Fernández et al. (2016) moves our $\mu(> t)$ curves closer to theirs. Limiting the optical fits to the same 3800–7000 Å range of their spectra further improves the agreement.

4.3 Global properties

In addition to the population vectors discussed above, STARLIGHT also returns global properties such as mass and dust attenuation; other properties like mean stellar ages and metallicities can be calculated by reducing the dimensionality of the population vector. Fig. 9 compares a series of these global properties derived with (y-axis) and without (x-axis) UV photometry. In order to highlight the general trends throughout the sample and give less weight to outliers, results are plotted as median curves with the region between 25 and 75% percentiles shaded in green. $\bar{\delta}$ and IQR values in each panel denote the median (bias) and interquartile region (scatter) of the difference between y and x values.

Panels (a) and (b) compare luminosity (at $\lambda = 5635\text{\AA}$) and mass weighted mean stellar ages, $\langle \log t \rangle_L$ and $\langle \log t \rangle_M$, respectively. In the case of $\langle \log t \rangle_L$ the bias is slightly positive ($\bar{\delta} = +0.04$ dex), and driven by the youngest systems, i.e., blue cloud galaxies, whose youngest populations shift from the $\log t = 6$ –7 range to the next decade ($\log t = 7$ –8) when UV constraints are used in the fits (see Fig. 8). Mass weighted log ages (Fig. 9b) are less sensitive to the recent SFH, thus spanning a much smaller range. Still, the negative bias of $\bar{\delta} = -0.04$ dex in $\langle \log t \rangle_M$ reflects how UV data leads STARLIGHT to bring down the contribution of the oldest stellar populations.

Panels (d) and (e) in Fig. 9 show luminosity and mass weighted log metallicities, respectively. UV data makes the most metal-poor galaxies become slightly less so, although overall biases is zero for $\langle \log Z \rangle_L$ and negligible for $\langle \log Z \rangle_M$

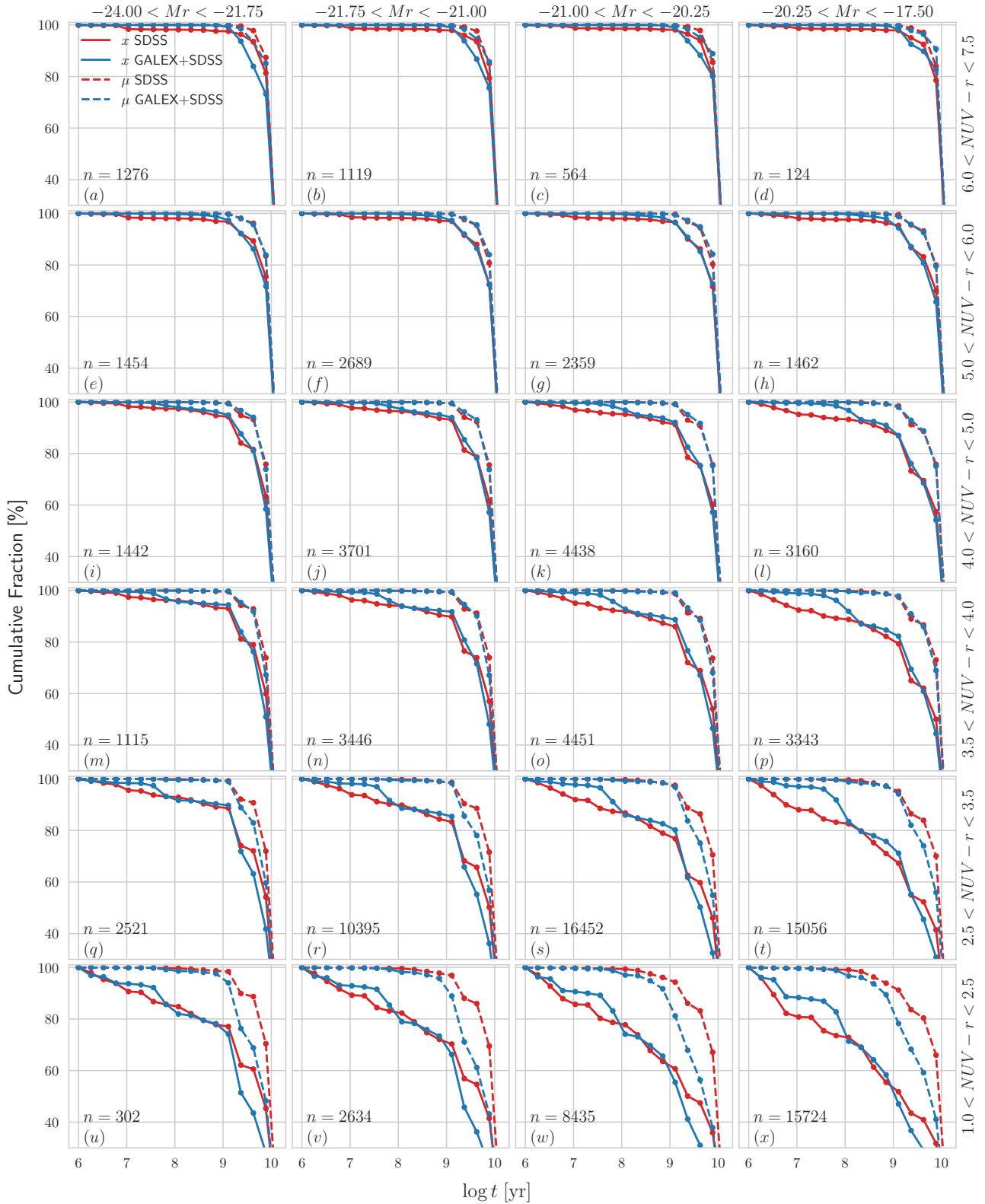


Figure 8. Average star-formation histories calculated with and without photometric UV constraints across the $NUV - r$ vs. M_r color-magnitude diagram. Solid lines show cumulative light fractions at $\lambda = 5635\text{\AA}$ while dashed lines show cumulative mass fractions. Red lines show results for pure SDSS fits and blue lines show results for combined GALEX+SDSS fits. Dots mark the edges of the CSP age bins. The number of galaxies in each bin (n) is indicated in the subplots.

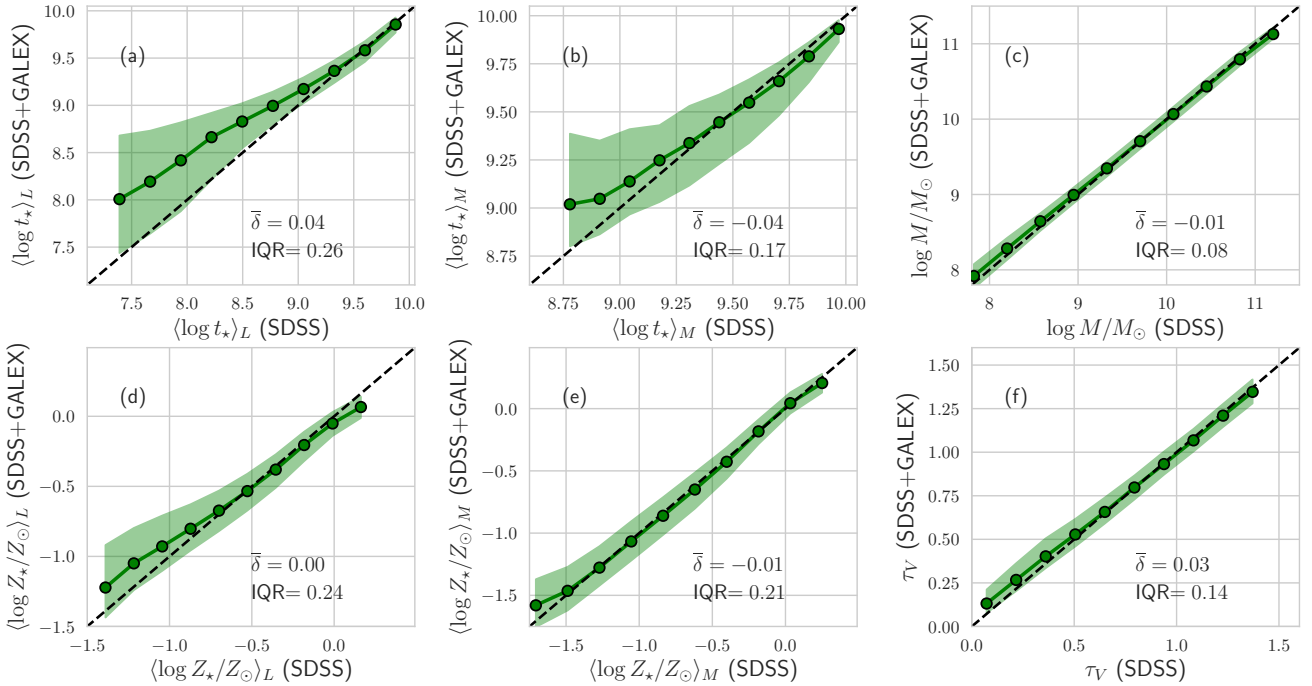


Figure 9. Comparison between galaxy properties derived with and without UV data. The y-axis corresponds to fits with UV constraints and the x-axis to fits to optical spectra, green lines show median curves with the center of each bin marked as a green dot with a black border. The region between 25 and 75% percentiles is shaded in green. Panels show mean stellar ages weighted by light (a) and mass (b), stellar masses (c), light (d) and mass (e) weighted mean stellar metallicities and V-band dust optical depth (f). Dashed black lines show a $y = x$ relation. Median $y - x$ values ($\bar{\delta}$) and interquartile (IQR) regions are annotated on each panel.

($\bar{\delta} = -0.01$ dex). López Fernández et al. (2016) find a larger negative bias in $\langle \log Z \rangle_M$, mostly due to late type, blue cloud galaxies, whose metallicities come out smaller in UV+optical fits. Again, this difference is due to differences in both data (mainly spectral coverage in the optical) and ingredients in the analysis (base models). Repeating the analysis mimicking their setup we reproduce their results.

UV constraints do not affect the estimates of stellar masses, as seen in Fig. 9(c). This is expected, given that we have seen that UV data mostly affects the youngest populations, which carry little mass. Somewhat more surprisingly, but in agreement with López Fernández et al. (2016), Fig. 9f shows that, in general, optical and UV+optical fits produce similar estimates of the dust attenuation, here converted to dust optical depth τ_V . This counter-intuitive result will be dissected in the following section.

The median curves in Fig. 9 highlight the general trends throughout the sample. As expected, there are points that fall out of this trend. This is the case for some galaxies with blue $NUV - r$ and relatively red $FUV - NUV$, a combination of colors that is sometimes achieved by reddening very young populations. When this effect is in place, the addition of UV data makes galaxies significantly younger and more reddened, deviating from the relations shown in panels (a), (b) and (f) of Fig. 9. This only happens for a small population of galaxies that bears no effect to the general trend, although this behavior is an interesting clue on galaxies that require two components of dust attenuation, which in principle could yield redder $FUV - NUV$, while having a smaller effect in $NUV - r$.

4.4 Effects on dust attenuation

As mentioned above, Fig. 9f bears the unexpected result that no significant change in dust attenuation is found with the addition of UV constraints. While true for the general population of galaxies, there can be important changes in τ_V for galaxies dominated by young stars. This effect gets diluted in Fig. 9, and its identification requires a more careful analysis.

A useful way to evaluate the sensitivity of our attenuation estimates to UV data is to investigate the relation between the far-UV attenuation (A_{FUV}) and the UV spectral slope (β , assuming $F_\lambda \propto \lambda^\beta$). This relation was originally found by Meurer et al. (1999) in a study of starburst galaxies⁴, and subsequently extended to larger and more diverse samples (Kong et al. 2004; Seibert et al. 2005; Buat et al. 2005; Burgarella et al. 2005). A general conclusion from these studies is that the correlation between A_{FUV} and β found for starburst galaxies becomes much more scattered for more quiescent systems, indicating that the SFH plays an important role in the relation.

To build the relation from our data, we estimate the UV spectral slope from the $FUV - NUV$ color using $\beta_{GLX} = 2.286(FUV - NUV) - 2.096$, as calibrated by Seibert et al. (2005). A_{FUV} is obtained from the Calzetti law, which gives $A_{FUV} = 2.53A_V$. In order to map the effects of the SFH we subdivide the sample into three bins in $\langle \log t_* \rangle_L$,

⁴ The relation also includes the ratio between far-infrared and UV luminosities (the IRX_λ), but this is not explored here.

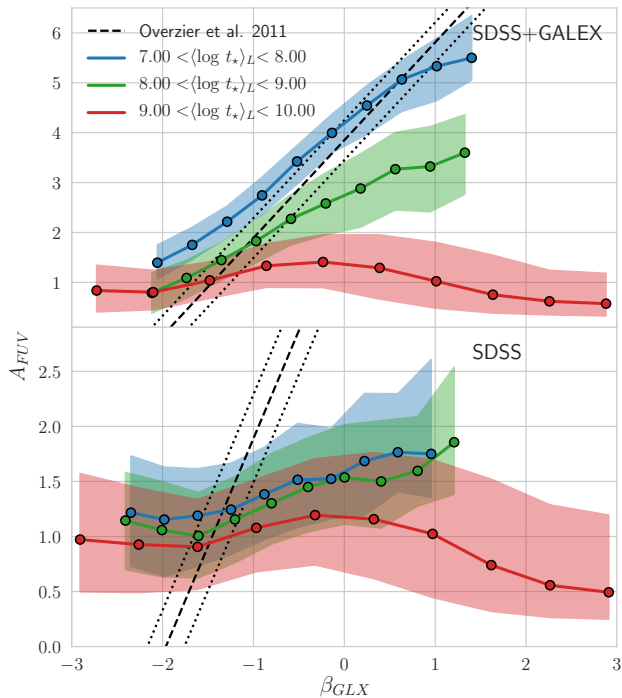


Figure 10. Relation between far-UV dust attenuation A_{FUV} UV power-law slope β for fits with (top) and without (bottom) UV data for three ranges of light-weighted mean stellar age $\langle \log t_* \rangle_L$. The relations are plotted as median curves with interquartile regions highlighted. Dotted and dashed lines represent the relation derived by Overzier et al. (2011).

luminosity-weighted mean log age (evaluated at 5635 Å, as in Fig. 9a).

The results of this analysis are shown in Fig. 10, where A_{FUV} is plotted against β_{GLX} . The top panel shows the relations for A_{FUV} obtained from SDSS+GALEX fits, while the bottom panel shows estimates of A_{FUV} derived from SDSS only. For comparison, we include the relation derived by Overzier et al. (2011): $A_{FUV} = 3.85 + 1.96\beta_{GLX} \pm 0.4$. In fits that include UV data, the relation is well reproduced in the younger age bin (analogous to starbursts), with a smaller slope for intermediate $\langle \log t_* \rangle_L$ systems and no correlation for galaxies dominated by old stars. Overall this confirms the previous suggestions that the SFH has a major impact on the relation between A_{FUV} and β .

For SDSS-only fits, on the other hand, the relations are much weaker and more scattered, with no significant change in slope from the first to the second age bin. Note also that the values of A_{FUV} estimated from SDSS+GALEX fits for star-forming galaxies are compatible with the ones presented in the literature (eg. Meurer et al. 1999; Seibert et al. 2005; Overzier et al. 2011), while the values obtained from SDSS-only fits are underestimated.

Finally, another important conclusion to be drawn from Fig. 10 is that changes in stellar populations are not sufficient for STARLIGHT to reproduce the $FUV - NUV$ colors of galaxies with significant amounts of young stars. In these cases, an increase in dust attenuation is also required.

5 APPLICATIONS

Having compared properties derived with and without UV constraints, this section focuses on the results obtained with our combined UV + optical synthesis analysis. The goal here is to explore some of the learning possibilities offered by this combined approach.

The broad spectral range of these fits calls for an explicit assessment of the λ -dependence of luminosity-based descriptors of the SFH. This is the subject of section 5.1, where the cumulative light fraction SFHs across the CMD of Fig. 8 are presented for a series of wavelengths from FUV to z . After that we address two unrelated example issues which benefit from our combined UV + optical analysis. Section 5.2 compares the SFHs of red-sequence ellipticals with (lined) and without (lineless) emission lines, in search for clues on why these otherwise similar galaxies differ in their emission line properties. Finally, section 5.3 explores whether our UV + optical analysis can shed light on the issue of which attenuation law best describes dust attenuation in galaxies of different types.

5.1 Wavelength-dependent star formation histories

STARLIGHT-based studies make abundant use of the luminosity-weighted mean log age $\langle \log t \rangle_L$ and SFHs expressed in terms of the light fraction population vector \vec{x} (e.g. Cid Fernandes et al. 2005; Mateus et al. 2006; Asari et al. 2007; Cid Fernandes et al. 2013). Although mass-based descriptions of the SFH are more directly comparable to models, light-based descriptions bear a direct and much stronger relation to observed properties which form the basis of our empirical knowledge of galaxy evolution.

By their very definitions, STARLIGHT's light fractions and light-weighted mean stellar ages are λ -dependent. Section 4, for instance, presented results for $x(t)$ and $\langle \log t \rangle_L$ for $\lambda = 5635 \text{ \AA}$, an arbitrary wavelength chosen for no fundamental reason other than being in a relatively clean, feature-free window. The purpose of this section is to take advantage of this λ -dependence, examining stellar populations in the wavelength ranges in which they are most relevant. Particular attention is given to the GALEX bands, as they present clear descriptions of stellar populations that are easily overlooked (or even undetected) in the optical.

5.1.1 Spectral algebra: Converting $\vec{x}(\lambda_0)$ to $\vec{x}(\lambda)$

Consider a spectrum $L_\lambda = \sum L_{j,\lambda}$ built by superposing $j = 1 \dots N_\star$ components $L_{j,\lambda}$, and let $x_j(\lambda_0) = L_{j,\lambda_0}/L_{\lambda_0}$ be the fractional contribution of the j^{th} component to the total emission at λ_0 . Each $L_{j,\lambda}$ can be written as

$$L_{j,\lambda} = L_{j,\lambda_0} \left(\frac{L_{j,\lambda}}{L_{j,\lambda_0}} \right) = x_j(\lambda_0) L_{\lambda_0} \left(\frac{L_{j,\lambda}}{L_{j,\lambda_0}} \right) \quad (4)$$

where $x_j(\lambda_0) \equiv L_{j,\lambda_0}/L_{\lambda_0}$ quantifies the contribution of component j to the total emission at λ_0 . The term in between parentheses can be expressed in terms of ratio of the intrinsic

sic (dust-free) luminosities, $b_{j,\lambda} \equiv L_{j,\lambda}^0/L_{j,\lambda_0}^0$, and the ratio of attenuation factors at λ and λ_0 , so that

$$L_{j,\lambda} = x_j(\lambda_0) L_{\lambda_0} b_{j,\lambda} e^{-\tau_j(q_\lambda - q_{\lambda_0})} \quad (5)$$

where τ_j is the V-band effective optical depth of component j , and $q_\lambda \equiv \tau_\lambda/\tau_V$ is given by the reddening curve. In practice $\tau_j = \tau$ if only one attenuation is allowed for, as in the case in this paper. Notice also that $b_{j,\lambda}$ are just the base spectra normalized at λ_0 .

But $L_{j,\lambda}$ can also be equated to $x_j(\lambda)L_\lambda$, where L_λ is the total emission and $x_j(\lambda)$ is the fractional contribution of component j to this total spectrum at wavelength λ . Comparing these two expressions for $L_{j,\lambda}$ leads to the sought relation between $x_j(\lambda)$ and $x_j(\lambda_0)$:

$$x_j(\lambda) = \frac{x_j(\lambda_0) b_{j,\lambda}}{\sum_j x_j(\lambda_0) b_{j,\lambda}}, \quad (6)$$

which allows one to convert the light fraction population vector from a chosen normalization wavelength λ_0 to any other λ .

5.1.2 Wavelength-dependent SFHs in the CMD

With equation 6, we calculated light fractions for all GALEX and SDSS bands. Fig. 11 shows the $x(> t, \lambda)$ cumulative light fractions as a function of age, as derived from our combined GALEX+SDSS fits. These λ -dependent descriptions of the SFH are broken into the same bins in the UV-optical CMD as in Fig. 8. Colors code for the reference wavelength, as labeled in the top-left panel.

The $x(> t, \lambda)$ curves for the longer wavelengths like the r, i, and z bands rise faster for more massive galaxies (left panels) than for those of lower mass (right), revealing the usual downsizing pattern. Because of the small influence of the young stars at these wavelengths these curves essentially reflect the mass growth curves previously shown in Fig. 8. At UV wavelengths, on the other hand, the light is always dominated by $< 10^8$ yr populations, and the curves are similar for galaxies of different masses. Relevant changes in the *NUV* and *FUV* curves occur only in the vertical direction, with the proportion of 10^{6-7} to 10^{7-8} populations decreasing as *NUV* – *r* becomes redder.

Panels (i) to (l) show galaxies in the green valley, mostly populated by an intermediate population of recently quenched galaxies moving from the blue cloud to the red sequence. Accordingly, all $x(> t, \lambda)$ curves shift towards larger ages. Unlike in the blue cloud, $> 10^8$ yr populations now contribute significantly even at UV wavelengths, particularly for the more massive galaxies.

Red sequence galaxies are shown in the top two rows of Fig. 11. For galaxies in panels (e) to (h), intermediate age populations are still relevant, while galaxies in the upper red-sequence (top row, panels a to d) are completely dominated by old stellar populations, even in the UV.

The evolutionary synthesis models used in this work become redder in *FUV* – *NUV* up to stellar ages of 1 Gyr. After that the model spectra become bluer in the UV, and after about 4 Gyr the stellar populations emit more *FUV* per M_\odot than immediately younger populations. This results

in a rise on the contribution of the oldest populations to *FUV* light, surpassing their contribution to the *NUV*. This tendency is connected to the UV upturn phenomenon, since at constant *NUV* – *r* the contribution of old populations to *FUV* light correlates with *FUV* – *NUV* color.

5.2 Liny and lineless retired galaxies

Up until now, we have used the UV-optical color-magnitude diagram as our guide to subdivide our sample into intelligible sub-classes. This diagram provides information on galaxy evolution and the bimodality of the local galaxy population. However, galaxies are complex systems, and no single diagram condenses all the information needed to describe them. Another popular way to divide the galaxy population is based on emission line diagrams. This type of classification separates galaxies with different sources of ionizing photons, an aspect that hasn't yet been touched in this work.

A popular emission line based classification is the one based on the $[\text{N II}]\lambda 6584/\text{H}\alpha$ flux ratio and the $\text{H}\alpha$ equivalent width ($W_{\text{H}\alpha}$), the so called WHAN diagram, introduced by Cid Fernandes et al. (2011). The main advantage of the WHAN diagram over those based solely on line ratios (e.g. Baldwin, Phillips & Terlevich 1981) is that it can identify retired galaxies (Stasińska et al. 2008, 2015). This diagram allows the identification of retired galaxies, characterized by having $W_{\text{H}\alpha} < 3 \text{ \AA}$. This class of galaxies can be misclassified as AGN in other diagrams, even though their ionization field is dominated by H0t Low Mass Evolved Stars (HOLMES) typical of old stellar populations.

Retired galaxies can be further subdivided into liny ($0.5 < W_{\text{H}\alpha} < 3 \text{ \AA}$) and lineless ($W_{\text{H}\alpha} < 0.5 \text{ \AA}$) systems, according to the presence or absence of emission lines. The fact that some retired galaxies lack emission lines poses an interesting astrophysical problem, since the HOLMES in both subclasses produce ionizing photons enough to power line emission. This problem is studied in detail by Herpich et al. (2018, hereafter H18). The aim of this section is to complement their analysis using our UV-optical spectral synthesis.

Through a pair-matching analysis, H18 were able to identify very small but consistent differences between the two sub-classes of retired galaxies. Compared to lineless systems, liny ones tend to be brighter in the GALEX *NUV* and WISE W3 bands, and have slightly smaller 4000 \AA breaks. These results are indicative of differences in dust content and SFHs. These differences in SFH, however, are hard to measure directly in the optical.

We have used our combined GALEX+SDSS spectral analysis to address this issue in the hope that a wider wavelength range leads to a clearer separation between the SFHs of liny and lineless retired galaxies. To this end, we have culled a sample of retired galaxies out of our low-*z* sample. In addition to the $W_{\text{H}\alpha}$ selection we also require the galaxies to be classified as ellipticals by Galaxy Zoo. Out of the 16206 retired galaxies in our sample, 12% are lineless and the remaining are liny.

Fig. 12 shows mean cumulative light fraction curves for lineless (top panels) and liny (bottom panels) galaxies, split into four bins of stellar mass. As in Fig. 11, each panel shows the $x(> t)$ curves for seven wavelengths corresponding to the GALEX and SDSS filters. Variations in the curves from left to right panels reflect the well known downsizing pattern,

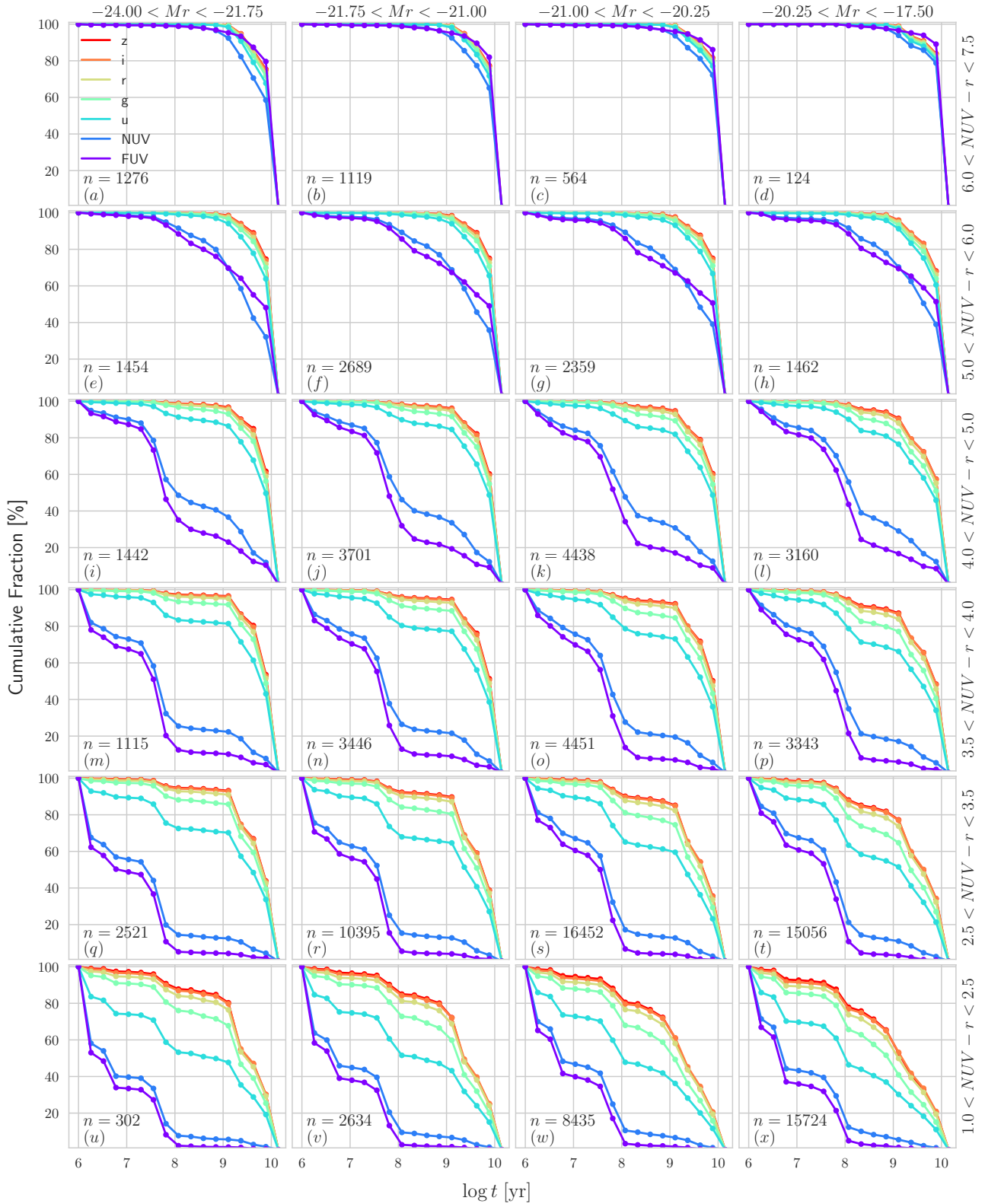


Figure 11. Average star formation histories for the same color-magnitude bins used on Fig 8, expressed as cumulative light fractions $x(> t, \lambda)$ in wavelengths corresponding to SDSS and GALEX bands. All curves correspond to results obtained in the combined GALEX+SDSS STARLIGHT fits.

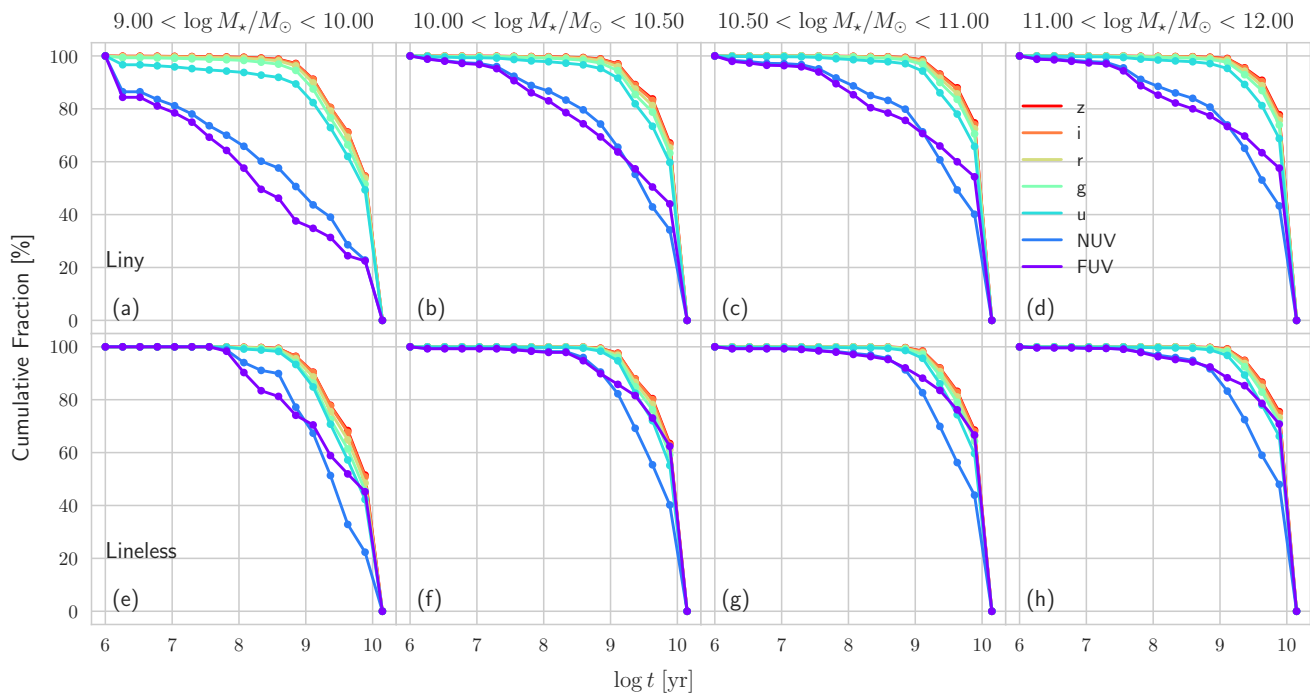


Figure 12. Wavelength dependent SFHs for liny (top row) and lineless (bottom row) retired galaxies divided into four mass ranges. Color codes are the same as in Fig 11.

with less massive galaxies having SFHs that are more extended in lookback time. The SFHs for the UV bands clearly show that liny galaxies experienced a more extended period of star-formation, a trend that is consistent in all mass ranges. The same signal is present in the $x(> t)$ curves for optical wavelengths, but at a much reduced amplitude.

Though populations of a few Myr may be present in low mass liny galaxies, the main difference is an excess of intermediate age populations (~ 0.1 – 1 Gyr). This directly shows that the presence or absence of emission lines in retired galaxies is connected to slightly different SFHs. H18 interprets this as due to an external reservoir of cold gas that is slowly accreted by liny galaxies, feeding a low level of star-formation over an extended period of time. In contrast, lineless systems exhausted their gas supply at an early epoch, leaving little or no gas to react to the ionizing radiation field produced by their HOLMES.

Another difference between these galaxy classes is the larger dust content in liny galaxies. The optical-only analysis on H18 is already capable of identifying higher τ_V values for liny galaxies at all mass ranges, a result that is confirmed here for both optical and UV+optical fits. Consistently with the H18 findings, we identify an average difference of $\Delta\tau_V = 0.15$ between liny and lineless galaxies.

5.3 Comparing results for different attenuation laws

Previous experiments with STARLIGHT found that spectral fits in the optical cannot distinguish among different choices of dust attenuation law. Asari et al. (2007), for instance, show that equally good fits are obtained with $q_\lambda = A_\lambda/A_V$ functions representative of the Milky-Way,

Magellanic Clouds, or starburst galaxies. This degeneracy is hardly surprising, given that the main differences between these alternative laws lies not in the optical, but in the UV.

One of the advantages of incorporating UV data in the STARLIGHT analysis is that it allows us to revisit this issue and investigate which dust attenuation law best fits the data. In this section we compare results obtained with the CAL and CCM laws, whose most notable difference is presence or absence of the UV bump at $\lambda \sim 2175$ Å. Given the overlap with the *NUV* filter, this feature is bound to affect our analysis. *FUV* fluxes are also affected by the choice of q_λ , given that the CCM law have a steeper far-UV slope, even though slopes in the optical are similar. Though the CAL and CCM laws do not span the wealth of dust attenuation effects studied in the literature (see Noll et al. 2009; Seon & Draine 2016; Salim et al. 2018; Narayanan et al. 2018), they serve as useful limits to investigate the effect of the bump. Moreover, they are both commonly used in STARLIGHT-based studies.

Qualitatively one expects fits using a CAL law to produce larger residuals in the UV than fits with a CCM law for galaxies with relevant UV bumps, and vice versa. It is therefore interesting to compare the UV residuals obtained with these two laws. To evaluate the quality of the fits in the UV let us use

$$\chi_{UV} = \sqrt{\frac{1}{2} \chi_{PHO}^2} \quad (7)$$

which gives an average of the *NUV* and *FUV* reduced residuals.

For this analysis we will restrict the sample to galaxies with $NUV - r < 5$ that are classified as spirals by Galaxy

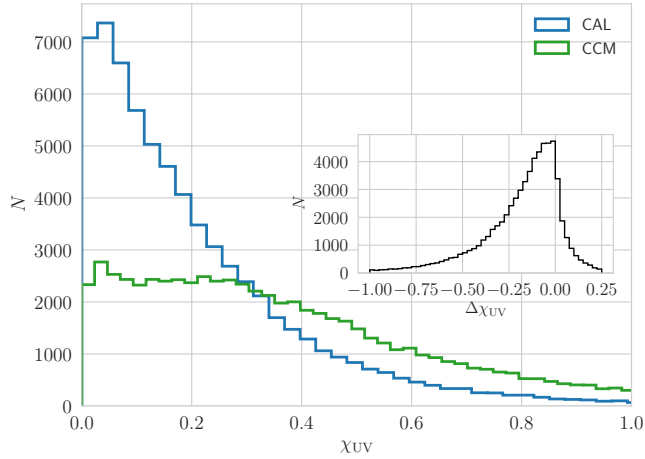


Figure 13. Histograms of χ_{UV} for the CAL attenuation (blue) and CCM extinction (green) laws. The inset shows the distribution of $\Delta\chi_{UV} = \chi_{UV}^{\text{CAL}} - \chi_{UV}^{\text{CCM}}$. Galaxies in these histograms are all Galaxy Zoo spirals with $NUV - r < 5$.

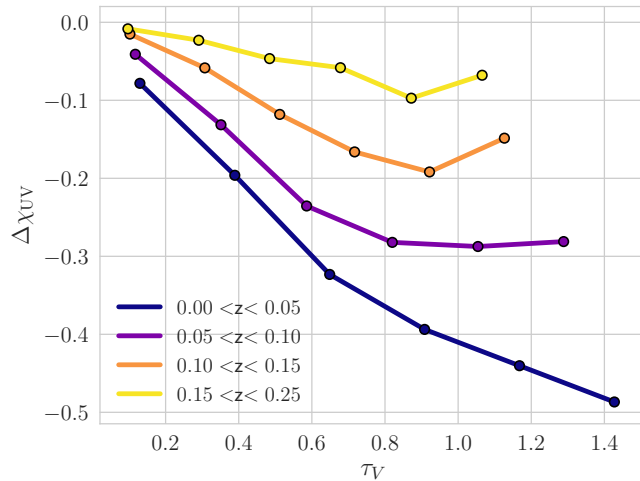


Figure 14. Median $\Delta\chi_{UV}$ plotted against dust optical depth τ_V in different bins of redshift. The center of the bins used to calculate the medians are indicated as points.

Zoo. On the other hand we do allow systems beyond $z = 0.1$ in order to trace the effect of the NUV band moving out of the UV bump region as redshift increases. These cuts yield a sample of 81214 galaxies.

Fig. 13 shows histograms of χ_{UV} for the CAL and CCM laws. The mean and rms values of χ_{UV} are 0.22 ± 0.26 for the CAL law and 0.41 ± 0.36 for CCM. The inset shows the histogram of $\Delta\chi_{UV} = \chi_{UV}^{\text{CAL}} - \chi_{UV}^{\text{CCM}}$. Over our whole sample $\Delta\chi_{UV}$ averages to -0.18 , showing that the CAL law is generally preferred over CCM.

We find that the main parameters controlling how worse the fits get with the CCM law are τ_V and redshift. Trends with mass and star-formation rate were also investigated, but we found no visible dependence of $\Delta\chi_{UV}$ with these parameters at fixed τ_V and redshift. In Fig. 14, we plot median curves of $\Delta\chi_{UV}$ as a function of τ_V for four different ranges in z . The τ_V values used in this plot are those derived from

purely optical fits with a CAL attenuation law, which are independent from the UV. The plot shows that, in comparison with CCM, the CAL law yields progressively better fits of the GALEX photometry as τ_V increases. The systematic behavior shown in Fig. 14 is expected to a certain degree, since the bump level is amplified as τ_V increases. Moreover, the quasi-universal relation between τ_V and the slope of the attenuation curve at any wavelength found by Chevallard et al. (2013) (and confirmed by Salim et al. 2018) also takes the results in this direction by favoring a steeper slope (MW-like) for low τ_V . The effects of redshift are also evident in this plot. At fixed τ_V , the $\Delta\chi_{UV}$ is largest (in modulus) at low redshift (blue curves in Fig. 14). As redshift increases the CAL and CCM laws yield increasingly similar χ_{UV} . We interpret this as due to the gradual shifting of the UV bump away of the NUV band as redshift increases. To first order this makes the two laws similarly bump-less, although differences in far-UV slope between the two q_λ functions persist.

Overall, the results in Fig. 14 indicate that the attenuation curves of the general population of spiral galaxies either lack the features that distinguish the MW extinction curve or exhibit them at a less significant level. This is compatible with other studies that generally find a small level of the bump both locally (Conroy et al. 2010; Wild et al. 2011; Salim et al. 2018), and at higher redshift (Kriek & Conroy 2013; Reddy et al. 2015). For instance, Buat et al. (2011) find an average bump amplitude of 35% the MW value for galaxies at $z > 1$. Similarly to our results, Battisti et al. (2016) find that the population of local star-forming galaxies can be described by a CAL-like law, but small levels of the bump cannot be discarded. This is not indicative, however, that the dust grain population in the MW is somewhat unusual, as recent models show that a bumpless attenuation law can arise even when the underlying extinction curve is MW-like (Narayanan et al. 2018).

Identifying a population of galaxies with relevant UV-bumps in our data-set is not straightforward, since the relation of $\Delta\chi_{UV}$ with attenuation is so strong that it contaminates other correlations. For instance, a key parameter in this analysis is galaxy inclination, but, since b/a correlates strongly with attenuation, plotting it against $\Delta\chi_{UV}$ would only show the reverberation of the correlation of both variables with τ_V . An attempt to isolate the effects of galaxy inclination in the shape of the attenuation curve is shown in Fig. 15, where we repeat Fig. 14 splitting the sample in four ranges of b/a . Edge-on galaxies are shown on the left and face-on ones on the right. As in Fig. 14, we are unable to identify a significant population of galaxies that is best fitted with the CCM law. That aside, a trend is clear in Fig. 15: fits with the CCM law get worse with decreasing inclination (increasing b/a).

This goes in the direction of the results of Conroy et al. (2010), although in that work it is found that a MW-like extinction law is required to fit the UV spectral slope of highly inclined galaxies, while we find only that these are the galaxies where MW law works best. Even in these cases our results are better for the CAL law. The relation of $\Delta\chi_{UV}$ with inclination is consistent with the idea that the shape of the MW extinction curve in the UV is associated with diffuse dust (Wild et al. 2011), while the CAL law is best-suited for birth clouds. As galaxy inclination increases, the amount of dust from birth clouds in our line of sight stays

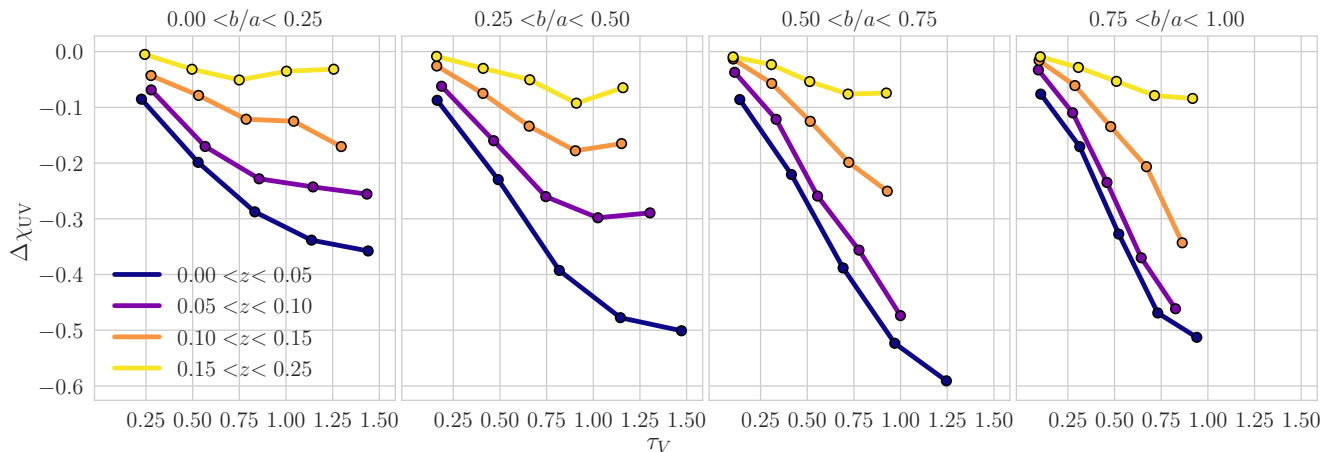


Figure 15. Median $\Delta\chi_{UV}$ plotted against dust optical depth τ_V in different bins of redshift in four ranges of inclination b/a . Edge-on galaxies are shown in the left and face-on galaxies in the right.

constant, while the column of diffuse dust increases. In this interpretation, highly inclined galaxies should show attenuation curves with shapes closer to the MW extinction law, as seen in Fig. 15. However, this result is not universal. For instance, the radiative transfer models of Pierini et al. (2004) show a decrease in the bump for edge-on galaxies.

Our analysis is sufficient to showcase the potential of combined SDSS+GALEX STARLIGHT fits in distinguishing between dust attenuation laws. A more thorough analysis, exploring laws with different slopes and bump strengths (e.g., Noll et al. 2009), as well as fits with a population-dependent dust attenuation (Charlot & Fall 2000) is deferred to a future study.

6 SUMMARY

We have developed a method to estimate GALEX UV magnitudes in apertures consistent with SDSS spectra. Tests indicate that this method produces very little bias, but considerable scatter, making it suitable for statistical analysis of large datasets, though not for individual sources. We also improved upon the version of STARLIGHT used by López Fernández et al. (2016), introducing a new method for combining spectroscopic and photometric figures of merit. Other improvements on the code remain under the hood as we work towards a public distribution of this new version of STARLIGHT.

We use the new code to simultaneously analyze SDSS spectra and GALEX photometry, retrieving stellar population properties of 231643 galaxies. Our overall results agree with previous work based on CALIFA+GALEX data, with few exceptions introduced by differences in stellar population models and spectral coverage. As seen in Fig. 5, with the addition of UV constraints STARLIGHT has to bring UV fluxes down without producing a redder optical spectrum. To achieve this, the code attributes larger light fractions to stellar populations with 10^7 to 10^8 yr, while cutting from the contribution of very young and very old stars to maintain optical colors. This behavior produces slightly older mean stellar ages when weighted by light, and slightly younger

when weighted in mass, as seen in Fig. 9. We also find an increase in dust attenuation for galaxies dominated by young stars (Fig. 10).

The panchromatic nature of our synthesis results was explored in section 5.1 by calculating wavelength-dependent star formation histories. As expected, UV light fractions are good tracers of recent star formation in the blue cloud, while optical bands are mostly tracers of old stellar populations. We also identify that UV light fractions are able to distinguish the stellar populations of liny and lineless retired galaxies, classes whose small differences in SFH are barely noticeable in the optical. In section 5.3, we showcase our ability to distinguish between attenuation laws of different shapes, while keeping a non-parametric analysis of stellar populations. Our results for the law of starburst galaxies of Calzetti et al. (2000) are systematically better than the ones for the MW law of Cardelli et al. (1989). A complete study on this topic, however, would have to include laws of different slopes and bump strengths.

The methodology of this paper provides galaxy properties derived from non-parametric spectral synthesis applied to optical spectra and UV photometry, expanding on previous STARLIGHT-based studies. The full potential of the dataset provided by our analysis is beyond what is explored in this paper, where we only presented short case-studies. Future applications may include a study of the UV upturn in elliptical galaxies and a deeper analysis of the shape of dust attenuation curves, as well as the effects of binary stars and differential dust attenuation to the UV.

ACKNOWLEDGEMENTS

The authors thank the anonymous referee for the valuable comments about the paper and especially for inspiring us to write section 4.4. AW would like to thank Andrew Battisti for the valuable discussions about GALEX+SDSS aperture matching schemes. AW, RCF, NVA and FRH acknowledge the support from the CAPES CSF-PVE project 88881.068116/2014-01. This study was financed in part by the Coordenação de Aperfeiçoamento de Pessoal de Nível

Superior – Brasil (CAPES) – Finance Code 001. NVA acknowledges support of the Royal Society and the Newton Fund via the award of a Royal Society–Newton Advanced Fellowship (grant NAF\R1\180403), and of FAPESC and CNPq. RGD thanks support from the Spanish Ministerio de Economía y Competitividad through the project AyA2016-77846-P. GB acknowledges financial support through PA-PIIT project IG100115 from DGAPA-UNAM. Funding for the SDSS and SDSS-II has been provided by the Alfred P. Sloan Foundation, the Participating Institutions, the National Science Foundation, the U.S. Department of Energy, the National Aeronautics and Space Administration, the Japanese Monbukagakusho, the Max Planck Society, and the Higher Education Funding Council for England. The SDSS Web Site is <http://www.sdss.org/>. The SDSS is managed by the Astrophysical Research Consortium for the Participating Institutions. The Participating Institutions are the American Museum of Natural History, Astrophysical Institute Potsdam, University of Basel, University of Cambridge, Case Western Reserve University, University of Chicago, Drexel University, Fermilab, the Institute for Advanced Study, the Japan Participation Group, Johns Hopkins University, the Joint Institute for Nuclear Astrophysics, the Kavli Institute for Particle Astrophysics and Cosmology, the Korean Scientist Group, the Chinese Academy of Sciences (LAMOST), Los Alamos National Laboratory, the Max-Planck-Institute for Astronomy (MPIA), the Max-Planck-Institute for Astrophysics (MPA), New Mexico State University, Ohio State University, University of Pittsburgh, University of Portsmouth, Princeton University, the United States Naval Observatory, and the University of Washington. This project made use of GALEX data and the Barbara A. Mikulski Archive for Space Telescopes.

REFERENCES

- Aihara H., et al., 2011, *ApJS*, **193**, 29
- Akritas M. G., Bershadsky M. A., 1996, *ApJ*, **470**, 706
- Aringer B., Girardi L., Nowotny W., Marigo P., Lederer M. T., 2009, *A&A*, **503**, 913
- Asari N. V., Cid Fernandes R., Stasińska G., Torres-Papaqui J. P., Mateus A., Sodr e L., Schoenell W., Gomes J. M., 2007, *MNRAS*, **381**, 263
- Baldwin J. A., Phillips M. M., Terlevich R., 1981, *PASP*, **93**, 5
- Battisti A. J., Calzetti D., Chary R.-R., 2016, *ApJ*, **818**, 13
- Bitsakis T., Bonfini P., Gonz alez-L opezlira R. A., Ram irez-Siordia V. H., Bruzual G., Charlot S., Maravelias G., Zaritsky D., 2017, *ApJ*, **845**, 56
- Bitsakis T., Bonfini P., Gonzalez-Lopezlira R. A., Ramirez-Siordia V. H., Bruzual G., Charlot S., Maravelias G., Zaritsky D., 2018, *VizieR Online Data Catalog*, **184**
- Blanton M. R., Roweis S., 2007, *AJ*, **133**, 734
- Blanton M. R., Kazin E., Muna D., Weaver B. A., Price-Whelan A., 2011, *AJ*, **142**, 31
- Bruzual G., Charlot S., 2003, *MNRAS*, **344**, 1000
- Buat V., et al., 2005, *ApJ*, **619**, L51
- Buat V., et al., 2011, *A&A*, **533**, A93
- Burgarella D., Buat V., Iglesias-P aramo J., 2005, *MNRAS*, **360**, 1413
- Calzetti D., Armus L., Bohlin R. C., Kinney A. L., Koornneef J., Storchi-Bergmann T., 2000, *ApJ*, **533**, 682
- Cappellari M., 2017, *MNRAS*, **466**, 798
- Cardelli J. A., Clayton G. C., Mathis J. S., 1989, *ApJ*, **345**, 245
- Carnall A. C., McLure R. J., Dunlop J. S., Dav e R., 2018, *MNRAS*,
- Charlot S., Fall S. M., 2000, *ApJ*, **539**, 718
- Chen Y., Bressan A., Girardi L., Marigo P., Kong X., Lanza A., 2015, *MNRAS*, **452**, 1068
- Chevallard J., Charlot S., 2016, *MNRAS*, **462**, 1415
- Chevallard J., Charlot S., Wandelt B., Wild V., 2013, *MNRAS*, **432**, 2061
- Cid Fernandes R., Gonz alez Delgado R. M., 2010, *MNRAS*, **403**, 780
- Cid Fernandes R., Mateus A., Sodr e L., Stasińska G., Gomes J. M., 2005, *MNRAS*, **358**, 363
- Cid Fernandes R., Stasińska G., Mateus A., Vale Asari N., 2011, *MNRAS*, **413**, 1687
- Cid Fernandes R., et al., 2013, *A&A*, **557**, A86
- Conroy C., 2013, *ARA&A*, **51**, 393
- Conroy C., Schiminovich D., Blanton M. R., 2010, *ApJ*, **718**, 184
- Falc on-Barroso J., S anchez-Bl azquez P., Vazdekis A., Ricciardelli E., Cardiel N., Cenarro A. J., Gorgas J., Peletier R. F., 2011, *A&A*, **532**, A95
- Fritz J., et al., 2017, *ApJ*, **848**, 132
- Gonalves T. S., Martin D. C., Men endez-Delmeestre K., Wyder T. K., Koekemoer A., 2012, *ApJ*, **759**, 67
- Gonz alez-L opezlira R. A., Bruzual-A. G., Charlot S., Ballesteros-Paredes J., Loinard L., 2010, *MNRAS*, **403**, 1213
- Gr afener G., Koesterke L., Hamann W.-R., 2002, *A&A*, **387**, 244
- Gutkin J., Charlot S., Bruzual G., 2016, *MNRAS*, **462**, 1757
- Hainich R., et al., 2014, *A&A*, **565**, A27
- Hainich R., Pasemann D., Todt H., Shenar T., Sander A., Hamann W.-R., 2015, *A&A*, **581**, A21
- Hamann W.-R., Gr afener G., 2003, *A&A*, **410**, 993
- Hamann W.-R., Gr afener G., Liermann A., 2006, *A&A*, **457**, 1015
- Herpich F., Stasińska G., Mateus A., Vale Asari N., Cid Fernandes R., 2018, *MNRAS*, **481**, 1774
- Koleva M., Prugniel P., Bouchard A., Wu Y., 2009, *A&A*, **501**, 1269
- Kong X., Charlot S., Brinchmann J., Fall S. M., 2004, *MNRAS*, **349**, 769
- Kriek M., Conroy C., 2013, *ApJ*, **775**, L16
- Lanz T., Hubeny I., 2003a, *ApJS*, **146**, 417
- Lanz T., Hubeny I., 2003b, *ApJS*, **147**, 225
- Lanz T., Hubeny I., 2007, *ApJS*, **169**, 83
- Leitherer C., Li I.-H., Calzetti D., Heckman T. M., 2002, *The Astrophysical Journal Supplement Series*, **140**, 303
- Leitherer C., Ortiz Ot alvaro P. A., Bresolin F., Kudritzki R.-P., Lo Faro B., Pauldrach A. W. A., Pettini M., Rix S. A., 2010, *ApJS*, **189**, 309
- Leja J., Johnson B. D., Conroy C., van Dokkum P. G., Byler N., 2017, *ApJ*, **837**, 170
- Lintott C. J., et al., 2008, *MNRAS*, **389**, 1179
- L opez Fern andez R., et al., 2016, *MNRAS*, **458**, 184
- Marigo P., Bressan A., Nanni A., Girardi L., Pumo M. L., 2013, *MNRAS*, **434**, 488
- Martin D. C., et al., 2007, *ApJS*, **173**, 342
- Martins L. P., Gonz alez Delgado R. M., Leitherer C., Cervi o M., Hauschildt P., 2005, *MNRAS*, **358**, 49
- Mateus A., Sodr e L., Cid Fernandes R., Stasińska G., Schoenell W., Gomes J. M., 2006, *MNRAS*, **370**, 721
- Meurer G. R., Heckman T. M., Calzetti D., 1999, *ApJ*, **521**, 64
- Narayanan D., Conroy C., Dave R., Johnson B., Popping G., 2018, preprint, ([arXiv:1805.06905](https://arxiv.org/abs/1805.06905))
- Nemmen R. S., Georganopoulos M., Guiriec S., Meyer E. T., Gehrels N., Sambruna R. M., 2012, *Science*, **338**, 1445
- Noll S., Burgarella D., Giovannoli E., Buat V., Marcellac D., Mu oz-Mateos J. C., 2009, *A&A*, **507**, 1793
- Ocvirk P., 2010, *ApJ*, **709**, 88
- Ocvirk P., Pichon C., Lanon A., Thi ebaut E., 2006, *MNRAS*, **365**, 74

- Overzier R. A., et al., 2011, *ApJ*, **726**, L7
- Panther B., Heavens A. F., Jimenez R., 2003, *MNRAS*, **343**, 1145
- Pierini D., Gordon K. D., Witt A. N., Madsen G. J., 2004, *ApJ*, **617**, 1022
- Rauch T., 2003, *A&A*, **403**, 709
- Rayner J. T., Cushing M. C., Vacca W. D., 2009, *ApJS*, **185**, 289
- Reddy N. A., et al., 2015, *ApJ*, **806**, 259
- Rodríguez-Merino L. H., Chavez M., Bertone E., Buzzoni A., 2005, *ApJ*, **626**, 411
- Salim S., 2014, *Serbian Astronomical Journal*, **189**, 1
- Salim S., Boquien M., Lee J., 2018, *The Astrophysical Journal*, **859**
- Sánchez-Blázquez P., et al., 2006, *MNRAS*, **371**, 703
- Sánchez S. F., et al., 2012, *A&A*, **538**, A8
- Sander A., Hamann W.-R., Todt H., 2012, *A&A*, **540**, A144
- Schlafly E. F., Finkbeiner D. P., 2011, *ApJ*, **737**, 103
- Schlegel D. J., Finkbeiner D. P., Davis M., 1998, *ApJ*, **500**, 525
- Seibert M., et al., 2005, *ApJ*, **619**, L55
- Seon K.-I., Draine B. T., 2016, *ApJ*, **833**, 201
- Stasińska G., et al., 2008, *MNRAS*, **391**, L29
- Stasińska G., Costa-Duarte M. V., Vale Asari N., Cid Fernandes R., Sodr e L., 2015, *MNRAS*, **449**, 559
- Stecher T. P., 1965, *ApJ*, **142**, 1683
- Todt H., Sander A., Hainich R., Hamann W.-R., Quade M., Shenar T., 2015, *A&A*, **579**, A75
- Tojeiro R., Heavens A. F., Jimenez R., Panther B., 2007, *MNRAS*, **381**, 1252
- Vidal-García A., Charlot S., Bruzual G., Hubeny I., 2017, preprint, ([arXiv:1705.10320](https://arxiv.org/abs/1705.10320))
- Walcher J., Groves B., Budavári T., Dale D., 2011, *Ap&SS*, **331**, 1
- Westera P., Lejeune T., Buser R., Cuisinier F., Bruzual G., 2002, *A&A*, **381**, 524
- Wild V., Charlot S., Brinchmann J., Heckman T., Vince O., Pacifici C., Chevallard J., 2011, *MNRAS*, **417**, 1760
- Witt A. N., Gordon K. D., 2000, *ApJ*, **528**, 799
- Wofford A., et al., 2016, *MNRAS*, **457**, 4296
- York D. G., et al., 2000, *AJ*, **120**, 1579